Bridging the Gap between Single Nanoparticle Imaging and Global Electrochemical Response by Correlative Microscopy Assisted By Machine Vision

Louis Godeffroy, Jean-françois Lemineur, Viacheslav Shkirskiy, Mathias Miranda Vieira, Jean-marc Noël, Frédéric Kanoufi

Bridging the gap between single nanoparticle imaging and global electrochemical response by correlative microscopy assisted by machine vision.

Louis Godeffroy, Jean-François Lemineur, Viacheslav Shkirskiy, Mathias Miranda Vieira, Jean-Marc Noël, and Frédéric Kanoufi**

L. Godeffroy, J.-F. Lemineur, V. Shkirskiy, M. Miranda Vieira, J.-M. Noël, F. Kanoufi
Université Paris Cité, ITODYS, CNRS, F-75013 Paris, France
E-mail: jeanfrancois.lemineur@u-paris.fr, frederic.kanoufi@u-paris.fr

Keywords: electrodeposition, electrocatalysis, correlative microscopy, machine vision

The nano-structuration of an electrochemical interface dictates its micro- and macroscopic behavior. It is generally highly complex and often evolves under operating conditions. Electrochemistry at these nano-structurations can be imaged both *operando* and/or *ex situ* at the single nanoobject or nanoparticle (NP) level by diverse optical, electron and local probe microscopy techniques. However, they only probe a tiny random fraction of interfaces that are by essence highly heterogeneous. Given the above background, correlative multi-microscopy strategy coupled to electrochemistry in a droplet cell provides a unique solution to gain mechanistic insights in electrocatalysis. To do so, a general machine-vision methodology is depicted enabling the automated local identification of various physical and chemical descriptors of NPs (size, composition, activity) obtained from multiple complementary *operando* and *ex situ* microscopy imaging of the electrode. These multifarious microscopically probed descriptors for each and all individual NPs are used to reconstruct the global electrochemical response. Herein the methodology unveils the competing processes involved in the electrocatalysis of hydrogen evolution reaction (HER) at nickel based nanoparticles (NPs), showing that Ni metal activity is comparable to that of platinum.

1. Introduction

Nano-structured electrochemical interfaces are now employed in many applications such as sensing, electrocatalysis or energy conversion and storage. [1,2] They are also very challenging to study because of the numerous heterogeneities hidden at the nanoscale. In particular,

considerable research efforts are devoted to the synthesis of novel nanomaterials presenting outstanding electrocatalytic activity. However, there are still difficulties in addressing properly structure-activity relationships in this field as they depend not only on intrinsic properties of the nanomaterials (size, geometry, surface chemistry,…) but also on their organization into a matrix assembled onto an electrode by mixing them with different extraneous components (e.g. carbon paste, binders,…). The latter micro to nanoscale matrix assembly is of paramount importance as it may tune the selectivity of electrocatalytic reactions upon appropriate control of the mass transfer regime.[3] In addition, the former intrinsic activity of nanomaterials is often fluctuating in operating conditions.[4] As a consequence, a unique and classical electro-analytical technique is not sufficient for fully characterizing the electrode nano-structuration that often results in complex electrochemical responses.

There is currently a general consensus on the need for standardized practices for the evaluation of the performances of electrocatalytic materials.[5–9] This need is indeed crucial when a myriad of new electrocatalyst formulations, ready to be benchmarked, can be quickly prepared by combinatorial synthesis of high entropy alloys.[10] Meanwhile, for electrocatalytic nanomaterials, recent studies point out the importance of *operando* characterization of surfaces at the ultimate spatial resolution[11,12] or at the single nanoparticle (NP) level[13–15] which, coupled to identical location complementary structural identification, can reveal intrinsic and local activity[16] while minimizing the electrode material complexity.

Advanced spatially resolved techniques, i.e. microscopies, allow recording information-rich nanoscale images and/or image sequences of nano-structured electrodes and electrode surface changes, when coupled *operando* or *post mortem* to electrochemistry.[17,18] However, they often provide limited information when operated separately. The challenge is therefore to correlate different microscopy approaches to unambiguously resolve structure, topography, composition and reactivity in the same nanodomain with the aim of revealing relationships

between those descriptors at the nanoscale. Typically, nanometer imaging resolution of electrocatalysts is afforded by different super-resolution scanning microscopes such as atomic force[11] or tunnelling[19] microscopes, or through the confinement of electrolyte droplets forming sub-30 nm nanoelectrochemical cells onto single electrocatalyst crystals.[10,16] The electrocatalytic activity of single NPs can be analyzed at higher throughput from the stochastic current transients associated to the reactive collision of individual NPs on a non-catalytic miniaturized electrode.[20,21] However, if electrocatalysis approaching the single atom resolution has been revealed by such strategy,[20] it usually requires nanoobjects that have a relatively narrow size distribution.[22]

Meanwhile, wide-field microscopies, such as optical microscopies with super-localization features, provide the highest imaging throughput of single NP electrochemistry.[23,24] Indeed, different optical microscopies are now able to see, in electrolytes and therefore under operating electrochemical conditions, many types of nanoobjects with sizes down to 10 nm.[24] As long as neighbouring NPs are separated by ca. 300 nm, they can be optically resolved enabling the optical monitoring of the electrochemical behaviour of a large set of single NPs. It can be employed to characterize the electrocatalytic activity of NPs through various optical signatures, attesting e.g. of the local change of refractive index by the electrogenerated products,[25–27] or the formation of nanobubbles of gaseous products.[28–30] Coupled with local electrochemical interrogation, e.g. a micro-sized electrolyte droplet confined on an electrode region, it allows visualizing a large set of (all) nanoobjects that are responsible of the electrochemical signature.[26,28,31,32] Such coupled methodology provides both the global electrochemical response of an ensemble of nanoobjects and the sum of all local individual nanoobjects. By bridging the gap between microscopic and macroscopic measurements,[12] it should provide a unique and complete (local to global,[33] or single to ensemble)[34] identification and quantification of electrocatalytic phenomena at the nanoscale.

Herein, we detail how this local to global electrochemistry approach can be employed. To do so, and as schematized in Figure 1, electrochemistry in a micro-sized droplet is coupled to different correlative microscopies with different resolutions, revealing electrochemistry at different scales, from the micrometer to the nanometer scale. First, an *operando* high temporal resolution optical microscopy is employed, which is then complemented by different *post-mortem* identical location high spatial resolution microscopies (scanning electron microscopy (SEM) complemented by energy dispersive X-ray spectroscopy (EDX), and atomic force microscopy (AFM)). The objective is to adapt the resolution of each technique so that by combining them all we reconstruct an image containing all the information from each of these techniques with the highest possible resolution (spatial, temporal and structural). The *operando* microscopy used here is a label free refractive index based optical microscopy, Interference Reflection Microscope, IRM,[35] however the methodology presented applies generally to any other (optical) microscopy available to image *operando* electrochemistry.[12,23,24,36–39] This methodology is made possible through the intensive assistance of machine vision concepts, such as border following, centroid finding, template matching and unsupervised machine learning algorithms. The latter is of particular interest since it deals with the unlabeled samples to reveal internal data structure and reduce data dimensionality, ruling out the possible human bias during data clustering.[40–42] Recent reviews in the fields of microscopy[43,44], atomic scale simulation,[41,45] biology,[40] etc. highlighted the power of unsupervised algorithms on the examples clustering of particle distributions, biological tissues and atomic structures, that is still, however, poorly exploited in electrochemistry.[39,42,46–48] Indeed, such automatized data treatment will provide various local descriptors for each (and all) nanoobjects imaged which can be used to reconstruct the global electrochemical response and in turns unveil the nanoscale contribution contained in an electrode response.

The interest of this strategy is herein demonstrated through the monitoring of the electrodeposition of nickel-based NPs, intensively studied due to their electrocatalytic activity.[49–52] Because of this catalytic activity, the mechanism of NP formation is also more complex as the Nickel (Ni) deposition reaction competes with water reduction that locally increases the pH and leads to local precipitation of $Ni(OH)_2$.[53,54] In turns, the formation of surface oxides or hydroxides should affect the elucidation of the intrinsic electrocatalytic activity of Ni NPs.

The interest of an *operando* imaging is that seeing it from the local (individual NP) and global perspectives, one can reveal more than just the sum of the individuals[34] and quantify the intrinsic electrocatalytic activity of metallic Ni NPs while they are produced. Owing to the high reactivity of Ni metal, this is a challenging measurement task. To the best of our knowledge, it was precisely addressed only through the surface interrogation mode of the scanning electrochemical microscopy (SI-SECM)[55] that allowed probing the catalytic activity of Ni metal when it is still very slightly oxidized.

2. Results and Discussion

2.1. Electrochemical Deposition of Nickel-Based NPs

As illustrated in Figure 1a, the experimental setup is a combination of a pipet-confined droplet electrochemical cell and a wide-field optical microscopy (IRM) in which an ITO coated glass cover-slip acts both as an optical sensor and as a working electrode for the electrochemical deposition of nickel. The pipet was filled with a Ni^{2+} containing solution, a Pt QRCE electrode was placed at the top of the pipet and then the pipet was approached to the ITO surface until a droplet cell of approximately 25 µm radius was formed. The whole area of the ITO surface wetted by the electrolytic droplet can then be monitored optically by illuminating from the backside through a 63x oil-immersion optical objective and collecting the light reflected by the droplet-ITO interface after passing back through the objective onto a CMOS

camera. A typical optical image of the ITO interface recorded under such reflecting condition is provided in Figure 1b and shows as the darkest oval region the droplet-ITO interface.

A Linear Sweep voltammetry (LSV) is performed at the working ITO micro-electrode confined by a 1 mM Ni^{2+} + 10 mM KCl containing droplet cell. Figure 1c represents the LSV obtained during a reductive potential scan engaging the electrodeposition of Ni at the ITO surface. At ca. -0.6 V, the current starts decreasing (denoted as 1 in the LSV of Figure 1c). This can be presumably related to the onset of the oxygen reduction reaction (ORR, equation 1) on the ITO surface:[32]

$$O_2 + 2H_2O + 4e^- \rightarrow 4HO^- \qquad (1)$$

Further decreasing the potential (step 2 in Figure 1c) leads to a peak at ca. -1.3 V related to Ni^{2+} reduction (equation 2).[53,56]

$$Ni^{2+} + 2e^- \rightarrow Ni \qquad (2)$$

The process is monitored optically at a frequency of 20 images per second and such *operando* optical observations confirm the electrochemical deposition of nanostructures, within the droplet region, detected in Figure 1b as bright contrasted features starting at ca. -1.1 V.

After sweeping the potential beyond the peak at ca -1.35 V, the current is finally decreasing again because of the solvent break-down, most likely catalyzed by the deposited Ni NPs. This current step is denoted as 3 in Figure 1c. The exact origin of the peak of the reduction current at ca. -1.3 V (step 2 in Figure 1c) is still not clear in the literature.[31] It was hypothesized that the current peak could be partly related to the two-electron reduction of Ni^{2+} into metallic nickel at the origin of the NPs' formation. However, the two-electron reduction of Ni also competes with the oxygen (equation 1) and water (equation 3) reduction reactions, that both locally increase the pH and favour the precipitation of $Ni(OH)_2$ (see equation 4).

$$4H_2O + 4e^- \rightarrow 4HO^- + 2H_2 \qquad (3)$$

$$2HO^- + Ni^{2+} \rightarrow Ni(OH)_2 \qquad (4)$$

Therefore, the rise in reduction current detected during step 2 in Figure 1c might also probe the onset of autocatalytic water reduction at the Ni NPs or $Ni(OH)_2$–coated Ni NPs, $Ni(OH)_2$ being known to enhance the catalytic activity of electrode materials.[51,52] This $Ni(OH)_2$ deposition reaction might be further inhibited as the layer of hydroxide blocks electrode charge transfer, explaining why the reduction current 2 rapidly drops.

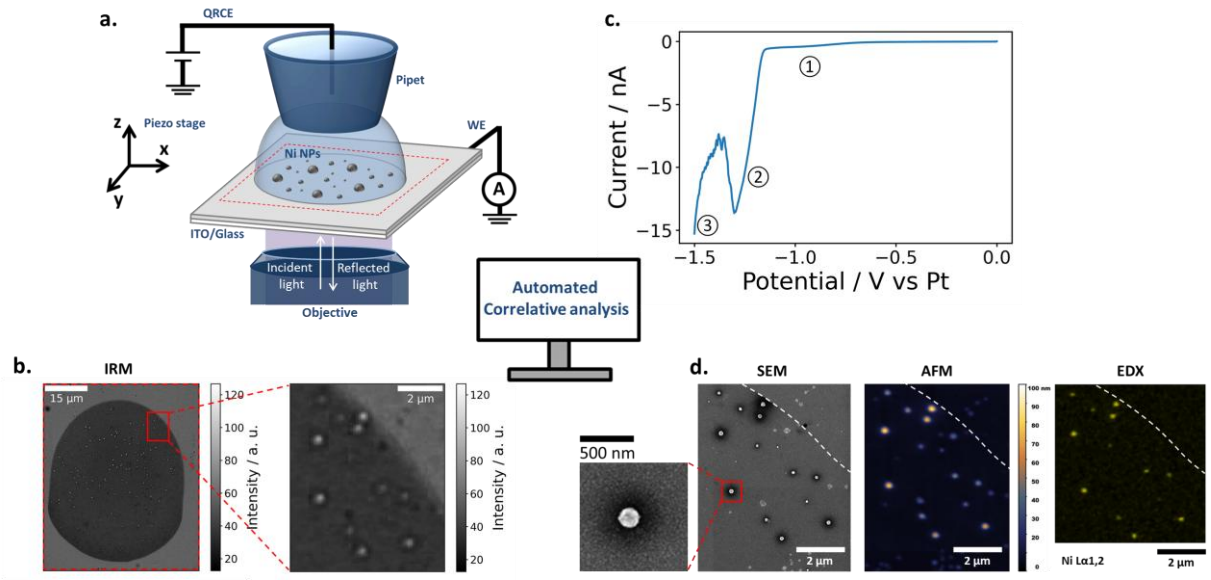

Figure 1. Correlative *operando*/*post mortem* multi-microscopy approach for probing Ni based NPs electrochemistry. (a) Schematic representation of the experimental setup used for probing the electrodeposition and electrocatalytic properties of Ni NPs from a 1 mM $NiCl_2$ + 0.1 M KCl electrolyte droplet confined onto an ITO electrode by a micropipet (ca. 50 µm in diameter). (b, c) *Operando* optical monitoring with (b) example (here at -1.5 V vs Pt) of the optical images (large field of view and region of interest at the droplet border) recorded during (c) a linear sweep voltammetry, LSV, from 0 to -1.5 V vs Pt at 100 mV/s. (d) *Ex situ* SEM (with enlarged view in single NP region), AFM and EDX maps of identical surface locations recorded *post-mortem* after the opto-electrochemical experiment.

To decipher the mechanism of Ni electrochemical deposition and the contribution of the competing reactions contained in the electrochemical signature, the *operando* optical images recorded during the LSV are extensively analyzed. These images assembled in a movie is provided in supporting information, SI, along with the Python program routines used to automatically analyze it. The positions of all the NPs in the optical images are localized and the evolution of their optical intensity is recorded during the whole experiment and at the single NP level. This procedure is named hereafter collecting single “optical transients” that

act as real time reporters of the NP's activity. Using optical modelling, it was possible quantifying from such optical transients the dynamic growth and electrocatalytic activity at the single NP level.[28,35]

Herein, the optical data collected for each NP are rather complemented with correlative identical location *post-mortem* SEM, EDX and AFM analyses, as illustrated in Figure 1d in a small region of interest (ROI). The structural data collected by such complementary images allow to fully unravel NP geometry and can be used, if properly correlated, as calibration procedure for optical measurement, making optical transients quantitative.[35]

2.2. Nanoscale reactivity

Color optical images were acquired during the LSV at a 20 Hz frequency and were synchronized with the potential ramp. The very first image is considered as the background and is subtracted from all other subsequent images. Each color image is split along its three color-channels and the red one is selected for data treatment as it presents the best signal to noise ratio. The last frame of the optical monitoring, recorded at -1.5 V, is shown in Figure 2a. It highlights the presence of NPs appearing as bright contrasted features.

The first descriptor to be evaluated from the optical images was the position of all newly formed NPs. Their exact locations in the droplet cell were extracted (Figure 2b, details in SI2) by an automatized procedure inspired from the Crocker and Grier centroid finding algorithm[57] and further refined to reach sub-pixel resolution (usually of ca. 1/10 pixel). The contour of the droplet cell was also retrieved using a border following algorithm[58] to sort optical features and systematically remove them if located outside of the droplet boundary. It is worth noting that the contour analysis run on all images in the sequence indicates there is no or negligible droplet expansion in the course of the EC experiment (See Figure SI2-1).

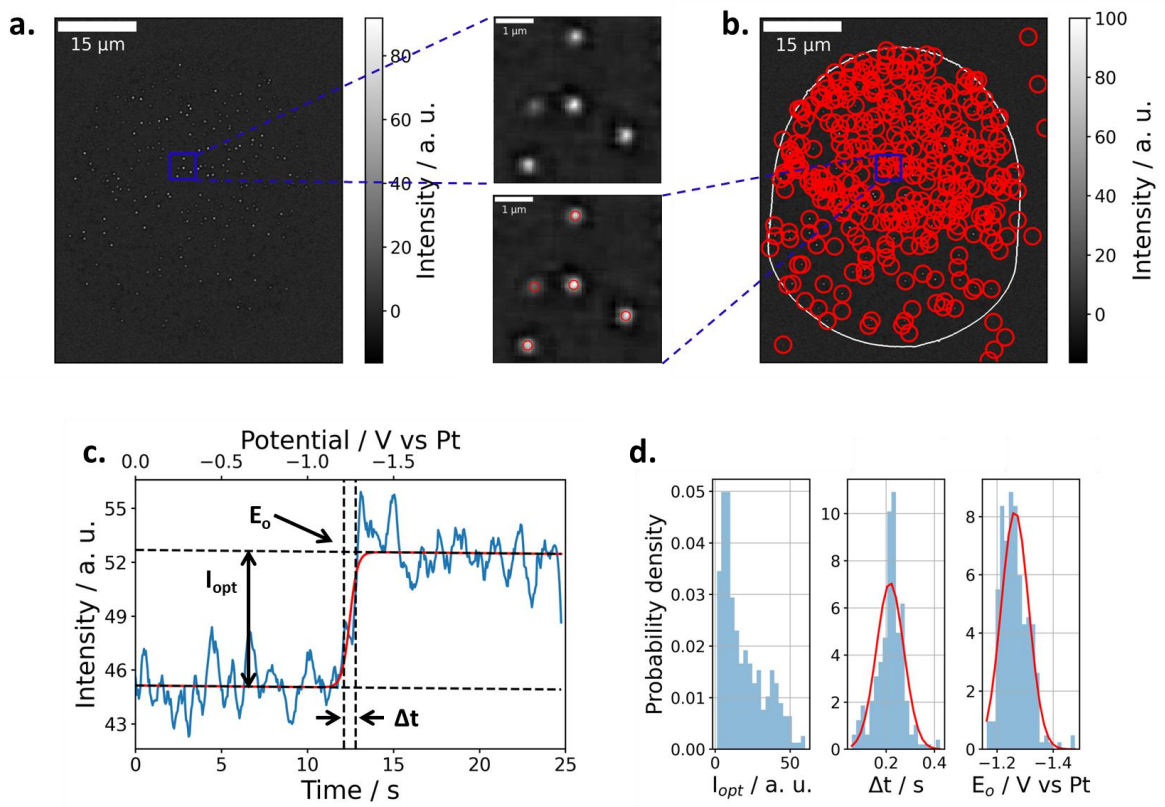

Figure 2. Automated NP detection procedures used to extract individual NP descriptors from *operando* optical images. (a) Background subtracted image of the ITO electrode (large field of view and region of interest) when polarized at -1.5 V during the LSV (see Figure 1). (b) Optical image (large field of view and region of interest) illustrating the droplet border localization and the detection of NPs by using the centroid finding algorithm, where each red circle refers to a localized optical mass and in which the droplet cell contour has been retrieved by a border following algorithm. (c) Example of optical transient from which three descriptors are extracted for a single NP; optical transient obtained by evaluating the change in pixel intensity in a 4x4 pixels ROI around the detected NP location. (d) Dispersion graphs of the NPs final background subtracted optical intensity (Iopt), growth time (Δt) and onset time (Eo) obtained from the temporal analysis described in (c) with best Normal distribution fit (red curve).

From the last image depicted in Figure 2b, the positions of 340 NPs were found, stored and further used as the anchor points in the next sections. At first sight, the NPs seem randomly deposited at the electrode surface with a rather homogeneous radial distribution.

A dynamic analysis is also conducted for each NP, as illustrated in Figure 2c. The local optical intensity fluctuations (i.e. optical transients) in each NP region (defined as a 4x4 pixels region centered on the stored NP coordinates) are collected, filtered and analyzed individually to finally extract three other essential NP descriptors: the NP final optical intensity (I_{opt}), the NP growth time (Δt) and the NP onset potential (E_o). The latter are illustrated in the transient

example of Figure 2c and summarized in the distributions of Figure 2d. I_{opt} corresponds to the maximum variation of the optical intensity from the instant when a single NP is detected on the image, emerging from the background, to the instant when its intensity reaches a steady value. The duration of this variation is noted Δt, while the instant the NP is first detected is the onset time, t_o, which is converted into an onset potential (E_o). I_{opt} is theoretically related to the final NP volume (V) from equation SI1 in SI. Similarly, Δt corresponds to the duration of the NP growth, and is then also related, as I_{opt}, to the final NP volume. The E_o distribution follows a Normal distribution, with a mean value of μ_{Eo}=-1.27 V, close to the peak potential detected in the LSV in Figure 1c (-1.30 V). Actually, the E_o distribution mimics the peak pattern in the LSV in Figure 1c, indicating that the onset of NP formation is indeed related to the onset of the reduction current.

2.3. Dimensions of NPs

The final NP size is evaluated by SEM. The characterization of the NPs structure is usually achieved by *post-mortem* electron microscopy analysis in a very small region of interest (ROI) and by considering the results representative of the whole nano-structuration. However, in order to correlate the final NP size with its optical descriptors (Δt and I_{opt}) and later evaluate the EC current associated to such NP growth or of structure-activity relationships at the single NP level, it is crucial to carry out a full *correlative* comparison between the optical and electron microscopy images. The method used is described below and the Python program routines used to perform such automatized task along with the different SEM images are provided and described in SI.

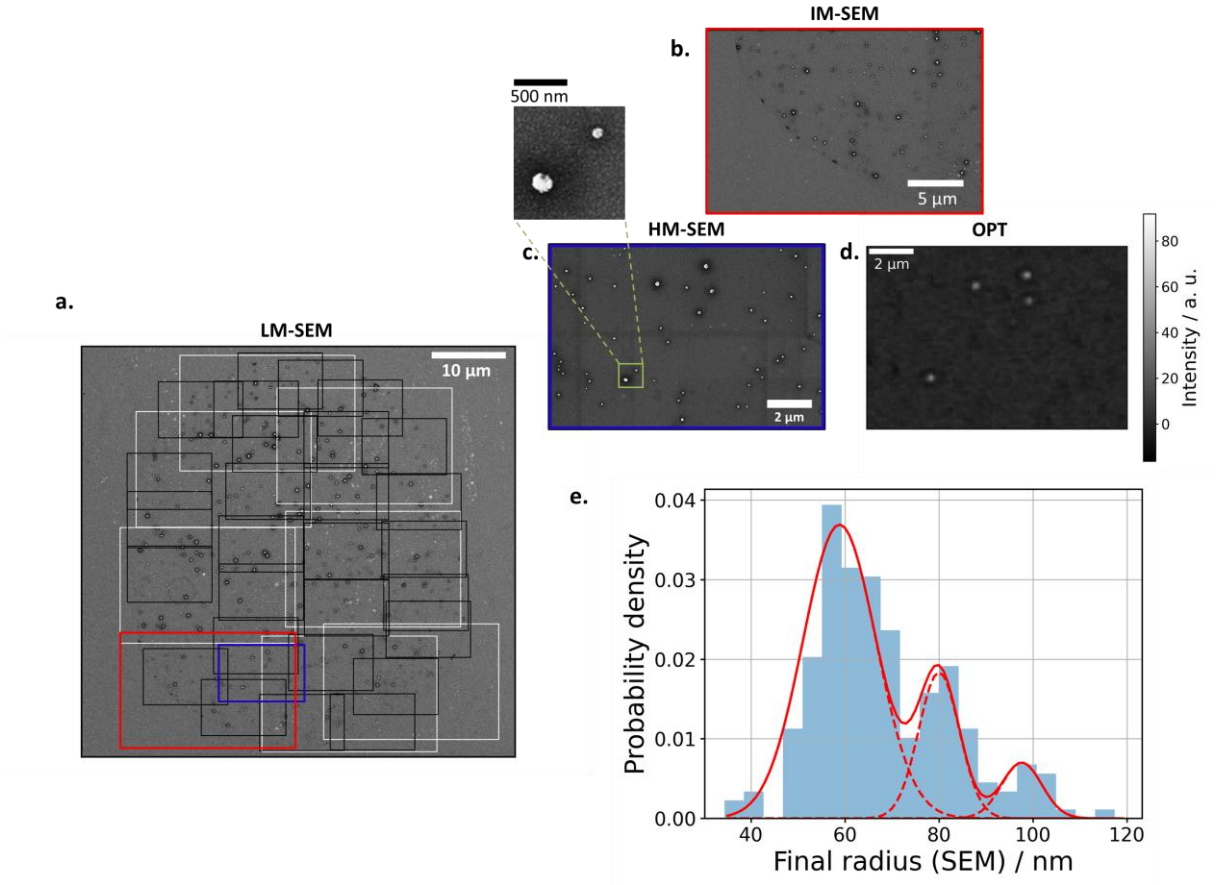

Figure 3. Automated feature based image alignment in optical and SEM microscopy for accurate identical localization (recognition) and sizing of individual NPs. (a) LM-SEM images of the droplet cell with the contours of intermediate, IM (white), and high, HM (black) magnification images overlaid after template matching. The collection of the IM and HM images constitute the images database used for NP sizing. (b) Example of IM-SEM image, (c) HM-SEM image (with enlarged view in NPs region) and (d) corresponding optical image. (b) and (c) can be located in (a) by using the color code. (e) Size dispersion graph of the NPs detected optically but measured from SEM images.

Herein, SEM at low magnification (LM) allows localizing the micrometric footprint of the droplet cell and the electrodeposited NPs in a relatively straightforward way. However, sizing the NPs by SEM requires acquiring high magnification images limiting the SEM field of view (FOV), or the SEM image size, and therefore greatly complicates the correlative approach. We then resorted to a template matching algorithm to localize and assess the size of all the NPs produced on the electrode.

Briefly, a database of higher resolution SEM images is constructed by acquiring intermediate (IM) and high-magnification (HM) SEM images within the droplet footprint to fully cover its

surface area. Then, the template matching algorithm was employed to overlay all HM and IM SEM images on the LM image (Figure 3a) and to prioritize them. In this way, a single NP selected on the LM image can be identified both in the IM image (Figure 3b) and in the most appropriate HM image (Figure 3c) from the images database. Once identified, its lateral size is extracted automatically with high accuracy (see Figure SI2-3 and description of sizing in SI). Finally, the optical and LM SEM images were correlated using reference NPs (positions known on both images), enabling to identify at high resolution the final lateral size of each optically detected NP. The automated comparison of the optical and electron microscopy images confirms that SEM reveals many more NPs than the bright contrasted features observed optically in the red color channel of the optical images. Actually, SEM detected exactly 919 NPs vs 340 NPs detected optically. The size dispersion graph of the NPs detected optically and sized by SEM is shown in Figure 3e.

2.4. Chemical composition of NPs

In previous studies, we have shown that the detection of NPs in the different color channels of the images as well as the optical contrast could significantly vary depending on the NP composition and size, offering an elegant way to distinguish NP compositional differences and to modulate the sensitivity of the optical method.[31] During the LSV, in addition of reducing Ni^{2+}, biasing the electrode negatively also causes local pH fluctuation that in turn lead to the precipitation of $Ni(OH)_2$ NPs which are detected rather as dark contrast features in IRM, as illustrated in Figure SI3. In addition, the ITO layer turned out to be very inhomogeneous, revealing under reductive conditions, nanoscale inclusions that can also be detected optically and that have been previously attributed to In NPs.[59]

Herein, the objective is to use SEM imaging, together with EDX analysis, to categorize all detected entities based on their chemical identity. A careful observation of the SEM images permits to highlight differences in NP contrast and morphology. Even if it is often subjective, human eye can here separate the NPs into three distinct categories: i) bright and smooth NPs,

ii) fractal NPs and iii) less contrasted NPs. Representative example images of each category constitute Figure 4a. Starting from these observations, we then performed a classification of the NPs based on their appearance in SEM images by means of agglomerative clustering belonging to unsupervised machine learning algorithms (the methodology is schematized in Figure 4b and explained in more details in SI, section SI4). It results in the identification of 4 distinct groups that are revealed from the principal component analysis visualized in the plot of Figure 4b. The belonging of each NP to one of the groups is indicated in the full-view LM and a zoomed HM SEM image by a color code presented respectively in Figure 4c and 4d. In each of the 4 groups all NP possessed identical chemical composition, identified in an independent EDX analysis of a limited (N= 20) but statistically representative number of each category. This strategy allowed us to avoid destructive and time-consuming EDX analysis of all NPs. It also permitted a further sub-classification of NPs based on their size.

One example of this correlative machine learning-SEM-EDX analysis is shown in Figure 4d. A closer look at the EDX spectra and especially at the Ni/O ratio also allows the identification of 3 types of NPs with distinct compositions lying at the electrode surface. First (i) two populations of metallic Ni NPs with mean radius of 72 ± 14 nm (noted as large) and 54 ± 7 nm (noted as small) nm are found. It is important to note that EDX spectra still revealed a small amount of O at these NPs location (O/Ni ratio is ca. 0.1) coming either from the ITO substrate or from the coating of the Ni NP by a $Ni(OH)_2$ shell. The two other categories are made respectively of (ii) $Ni(OH)_2$ NPs with a O/Ni ratio greater than 0.5, and (iii) ITO nano-heterogeneities, often associated with the formation of In NPs,[60,61] and for which no Ni is detected.

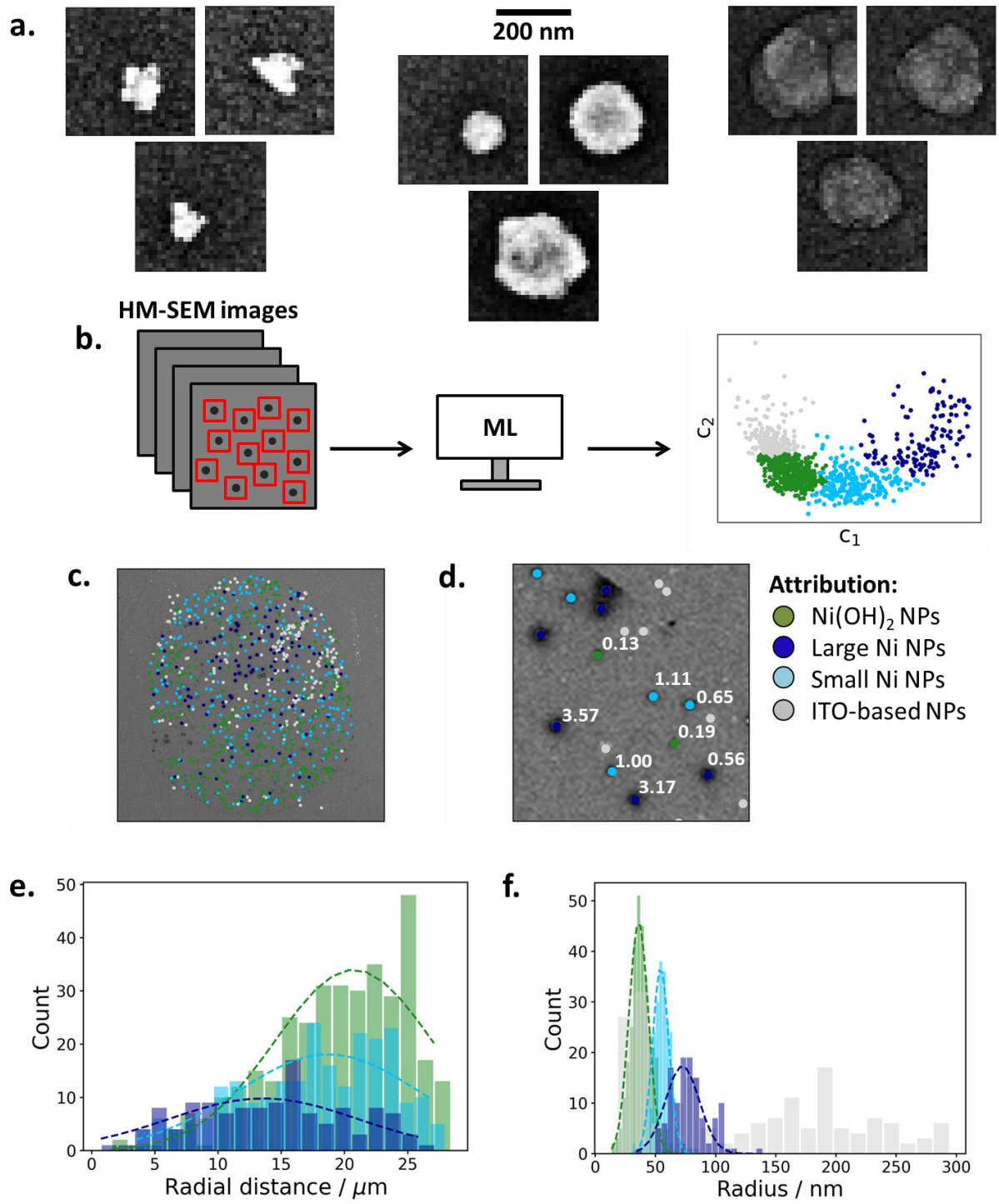

Figure 4. Agglomerative clustering by size and chemical composition of electrogenerated NPs from SEM-EDX analysis. (a) Examples of the three types of NPs that can be distinguished from the database of *post-mortem* SEM images defined in Figure 3. (b) Schematic representation of the agglomerative clustering procedure used for the NPs classification. Individual NP crops are flattened and the two first principal components are computed before being processed by the Ward's algorithm. (c) and (d) Chemical attribution to each NP detected in the SEM images based on the results given by the agglomerative clustering. (c) LM SEM image illustrating the spatial arrangement of the classified NPs. Yellow, purple, green and blue correspond to $Ni(OH)_2$ NPs, large Ni NPs, small Ni NPs and ITO in-homogeneities, respectively. (d) HM SEM image with chemical attribution and Ni/O ratio

obtained by EDX analysis. (e) Radial distributions for the Ni-based NPs. (f) Size dispersion graphs for each NPs group based on SEM images.

The light and dark blue dots corresponding to small and large metallic Ni NPs, respectively, account for 40 % of all the NPs that is 364 NPs. This number is in fairly good agreement with the number of NPs optically detected as bright contrasted features (N=340, 93 %) and that have been previously assigned to metallic Ni NPs.[31] It indicates that the optical microscopy detected most of the electrodeposited Ni NPs, and definitely all the largest Ni NPs that should contribute the most to the Ni reduction current.

The green dots population is the most represented one (N = 349 NPs) and corresponds to $Ni(OH)_2$ NPs formed upon precipitation of Ni^{2+} ions associated to competing water or oxygen reduction. It is interesting to note that these green dots seem spatially separated from the large Ni NPs (*i.e.* the dark blue population). One of the reasons for such segregation could be that Ni electrodeposition competes with water or oxygen reduction on the ITO electrode. Therefore, when these parasitic reduction reactions are predominant, only small metallic Ni NPs nucleate, while larger Ni NPs are present in regions where water reduction is inhibited. $Ni(OH)_2$ NPs are also located closer to the border of the droplet cell, where oxygen diffusion is believed to be accelerated. This preferred localization of the $Ni(OH)_2$ and small Ni NPs within the droplet edge is more clearly visible in Figure 4e that represents the radial distribution of the different NP populations. If large Ni NPs are largely distributed covering homogeneously the whole droplet positions, the small Ni and $Ni(OH)_2$ NPs are more massively found 20-25 µm from the droplet center. It suggests that the oxygen reduction reaction (ORR) is most likely the main contribution to the pH fluctuations near the edges yielding local $Ni(OH)_2$ NP precipitation. This conclusion about the importance of ORR at ITO is in line with the visualization of the electrochemically triggered crystallization of $CaCO_3$[32] and is further optically confirmed by the appearance of $Ni(OH)_2$ NPs during the ORR wave (1) along the LSV (see Figure SI3 for more details).

One can also notice that ITO heterogeneities are also separated from the $Ni(OH)_2$ NPs. This competition between parasitic reduction reactions is ruled out by the electrode (i.e. the ITO layer) composition and its ability to trigger one of the reactions. A similar behaviour has been recently evidenced for the competition between ITO reduction reaction and hydrogen nano-bubbles nucleation at the very same ITO electrodes,[59] or from the nanoscale imaging of the heterogeneous electrochemical activity of ITO surfaces.[62–64]

2.5. From local nanoscale descriptors to global electrochemistry

From the descriptors extracted from the temporal analysis, the NPs size can be inferred. Owing to the low density of metallic Ni NPs on the electrode surface, the growth of each NP can be considered independent, or isolated, from its neighbours.[65–67] The electrochemical growth of each NP then occurs by steady-state hemispherical diffusion of Ni^{2+} ions to a 3D nanoscale collector (the NP). It is thus possible to derive the dynamic evolution of the NP size during its growth (details in SI, section SI2) from the expression of the diffusive flux to a 3D collector.[68,69]

The final size r_{max} of each NP can then be inferred from its characteristic growth time Δt:

$$r_{max} = (2fCV_mD)^{0.5}\,(\Delta t + \Delta t_{LOD})^{0.5} \qquad (5)$$

where, C and D are respectively the bulk concentration and diffusion coefficient of Ni^{2+}, V_m the molar volume of metallic Ni. f and Δt_{LOD} are correction factors. Δt_{LOD} describes the limit of detection of the optical microscope. It corresponds to the time difference between the onset of the nucleation of the NP and the initial detection of its optical footprint (see SI section SI1 and SI5 as well as Figure SI2-4). It is at first considered constant for all NPs. On the other hand, f accounts for the influence of the 3D geometry of the NP on its diffusional flux and its expression can be computed by finite elements modeling, or found in the literature (see section SI6 for more details).[70,71]

The f pre-factor estimate requires a precise knowledge of the NP geometry. Unfortunately, the SEM inferred NP radius, r, is not fully sufficient to characterize the 3D geometry of a NP, as

electrodeposition processes often result in spherical caps with a height, h, different from their projected diameter (determined by SEM). Herein, the precise evaluation of NP height is obtained by AFM images, at identical location, of the sample. A full 3D geometrical description of several (N=15) NPs is then obtained by correlative SEM-AFM analysis (Figure 5a and 5b, see also Figure 1d for a second example of correlative analysis), where SEM provided the projected diameter of the NPs and AFM their height. Note that the automatized alignment for identical location analysis of the AFM image with the SEM (or/and optical) image can be made by implementing the procedure (and corresponding scripts given in SI) described in Figure 3. Results of r vs h correlation are shown in Figure 5b for the same individuals. For all NPs, the height imaged by AFM varies linearly with the projected radius r, indicating that all NPs have the same aspect ratio, h/r, and therefore produce the same contact angle with the electrode surface. The height h is smaller than the corresponding projected radius r, indicating, as schematized in Figure 5c, that the contact angle, θ, is lower than 90°. For θ<90°, or equivalently if h<r, the contact angle can be estimated from the slope in Figure 5b and by using equation (6),

$$\theta = 2\,\mathrm{atan}\left(\frac{h}{r}\right) \qquad (6)$$

an average value of the NP contact angle of ca. 75° is obtained. Then, f is calculated and amounts to 1.25 based on the data published in the literature (details in SI, section SI5).[71] The dispersion graph resulting from the NP growth model calculated by means of the optical growth time Δt is presented in Figure 5d. As detailed in SI, a Δt_{LOD} = 0.04 s, corresponding to a delay of less than one optical frame, was used.

The optically inferred mean NP size is in excellent agreement with the one directly measured by SEM analysis. However, the SEM size distribution (Figure 3d) is also broader and reveals the presence of (N=60, i.e. 16.5 %) large NPs with r > 80 nm. If one considers that such large NPs could not be explained from the above diffusion-controlled growth model, they should

most likely be produced from the merging of multiple NPs growing from different neighboring nucleation sites.

Such NP assembly was demonstrated from *ex situ* identical location electron microscopy dynamic monitoring of electrodeposition processes.[72,73] A clustering comparison of the final NP volume estimated from SEM and from the diffusion model shows in Figure 5e that the larger NPs revealed by SEM correspond to the merging of 2 or 3 NPs, suggesting their formation through 2 or 3 nucleation sites. Optical methods do not have the resolution to resolve such phenomena *in situ*. However, neither the *post mortem* SEM analysis could evidence it. Noteworthy, its occurrence is supported by the multi-correlative approach proposed here.

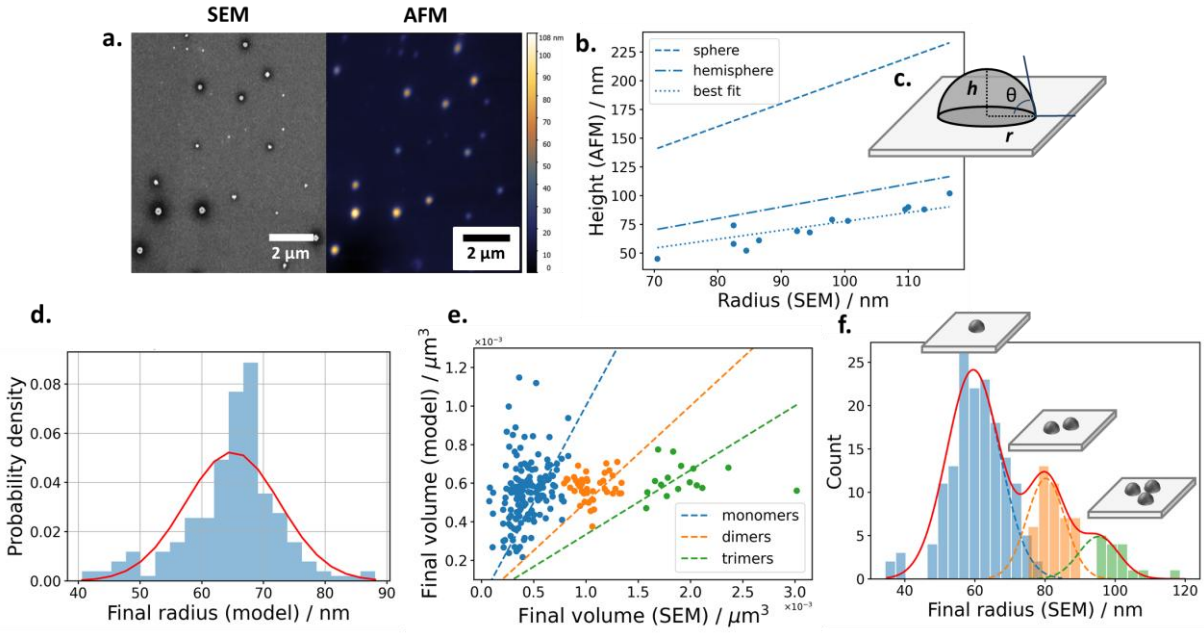

Figure 5. Evaluating the 3D growth dynamics of Ni NPs. (a) Correlative SEM and AFM analysis in a ROI of the droplet cell allowing to infer (c) the NP contact angle by correlating (b) the AFM-measured NP height and its SEM-measured projected radius. (d) Dispersion graph of the modeled NP size obtained from the optically determined NP growth descriptors (Figure 2c) and a diffusion-controlled growth (equation 5). (e) SEM vs modelled NP volume clustering highlighting the NP growth from 1, 2 or 3 independent nuclei. (f) Size dispersion graph of the NPs optically probed but measured and clustered from SEM images.

The structural descriptors (i.e. r, h and θ, or equivalently NP volume, V, chemical composition) obtained by SEM and AFM now complement mechanistic descriptors (growth

duration Δt and onset time t_o, 1 to 3 nucleation sites) obtained by applying a growth model to the dynamic optical monitoring. They can be exploited to reconstruct the electrochemical (LSV) current flowing through the droplet cell related to nickel deposition (i_d). It has been achieved by evaluating the time derivative of each Ni NP volume (V) and summing over all NPs detected, as in equation 7.

$$i_d = -2\frac{F}{V_m}\sum_{NP} n_n \frac{dV_{opt}}{dt} \qquad (7)$$

where F is the faraday constant and V_{opt} is the volume of each Ni NP at instant t derived from the growth model and n_n the number of nuclei the NP is made of (n_n=1, 2 or 3).

This optically-inferred current i_d is plotted in Figure 6a as a function of time and is compared to the baseline subtracted total experimental current (i_{exp}) collected by the potentiostat during the electrochemical deposition. There is a clear mismatch between both currents, the experimental one being about 3-4 times larger than the optically inferred one. This is confirmed from a coulometric analysis, without the need to rely on any model. The total charge used for the Ni NP formation can be precisely evaluated from the accurate NP sizing by *post-mortem* SEM and AFM analyses and Faraday's law, yielding a calculated charge of 4.8 nC. This value is again much smaller than the charge calculated by integrating the experimental LSV peak which is equal to ca. 17.1 nC.

From both the optically inferred growth model and *post mortem* SEM, the charge or current mismatch stresses another source of electron flow during Ni NP formation. One could incriminate the formation of some of the many (N=349) $Ni(OH)_2$ NPs detected by SEM. These $Ni(OH)_2$ NPs act as nanoscale reporters of the electrode catalytic activity through equations 1, 3 and 4. Considering their sizes and number, their formation corresponds to a total catalytic charge of 0.7 nC, according to an electron/hydroxide anion ratio equal to 1. This value is negligible compared to the charge mismatch (12.3 nC) between the charge required for the growth of all Ni NPs and that estimated from the LSV. The charge mismatch

is then believed to originate from the electrocatalysis of another reduction process, likely, as schematized in Figure 6c, water reduction, operating during the Ni NPs formation at the Ni metal surface.

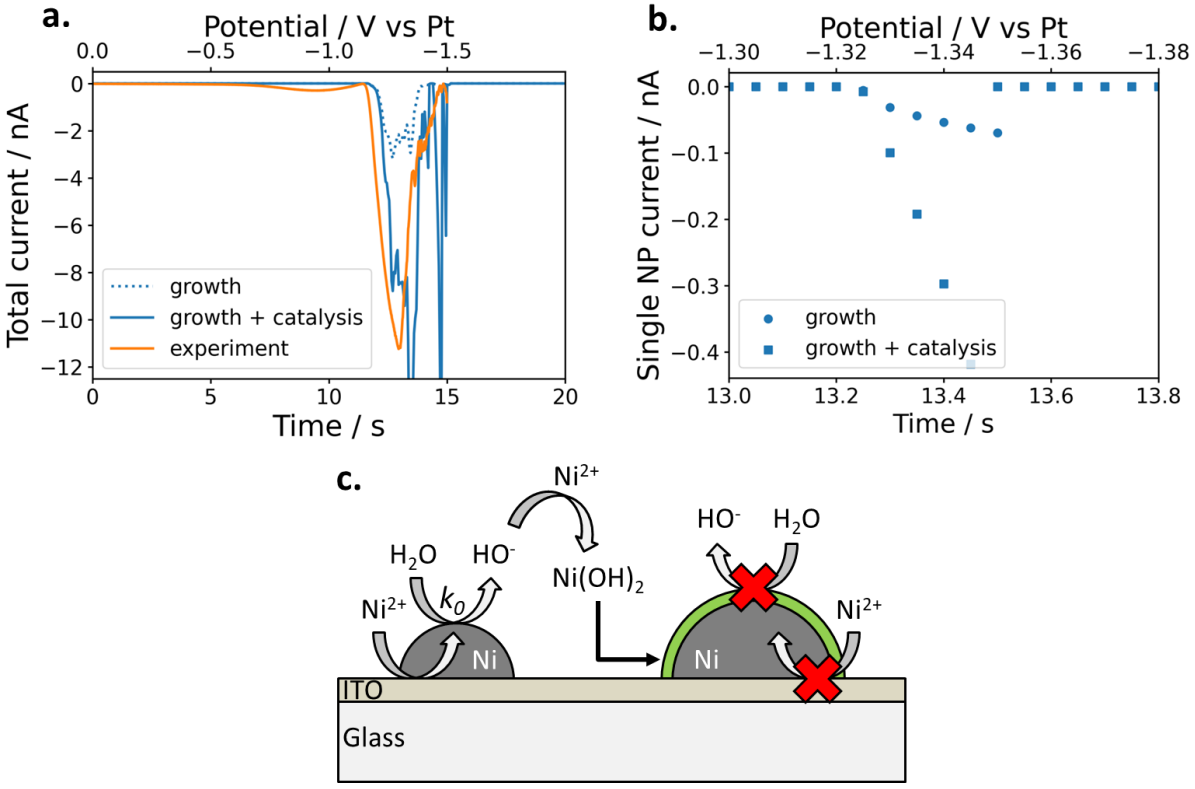

Figure 6. Evaluating the contribution of HER electrocatalysis in the electrochemical response from single NP growth dynamics. (a) Comparison between the electrochemical current recorded by the potentiostat (background subtracted) and the total modeled current for Ni NP growth and electrocatalysis ($i_d + i_{cat}$) considering the growth dynamics adjusted from optical monitoring and SEM sizing. (b) Modelled current transients for an individual NP growth and electrocatalysis using the same comparison as for (a). (c) Mechanistic scheme used to evaluate the rate constant k_0 of the H_2O electrocatalytic reduction at metallic Ni NPs.

Consequently, the charge mismatch should reflect the extent of the electrocatalysis of water at freshly deposited Ni metal NPs. The charge mismatch should allow us to estimate the rate of this electrocatalytic reduction with the help of a few approximations. i) As a result of the self-terminated NP growth, it is assumed that water reduction only occurs during NP growth at the metallic Ni NP surface. ii) The electrocatalytic activity is similar for all NPs and does not fluctuate with NP size; it is characterized by a heterogeneous rate constant k_0 (in cm/s). iii)

The rate-limiting step is the Volmer step as previously stated.[55] Then, one could express the electrocatalytic current from the contributions of all NPs by equation 8.

$$i_{cat} = -F \sum_{NPs} k_0 A_{opt} e^{-\alpha F(E-E_0)/RT} \quad (8)$$

where A_{opt} corresponds to the area of a given NP, evaluated from the growth model (see SI section 6 for its expression), α and ($E-E_0$) are the charge transfer coefficient and the over-potential for water reduction on Ni, respectively. R and T stand for the molar gas constant and the temperature, respectively. E is the onset potential derived from one of the descriptor obtained by the temporal analysis.

A good overlap between i_{exp} and ($i_d + i_{cat}$) is obtained for k_0 equal to ~ 6.5 10^{-5} cm/s, as shown in Figure 6a. This value is in fairly good agreement with the value obtained by Bard and co-worker in 2017,[55] employing the surface interrogation mode of the scanning electrochemical microscopy in combination with Tafel analysis, when considering k_0 is calculated with water activity equal to 1 M. In addition, using the exact same methodology and the microscopically inferred k_0, the current related to the growth and catalysis can be inferred at the single NP level. One example is presented in Figure 6b for a NP with final radius of 96 nm. Noted that a closer examination of Figure 6a tends to suggest that k_0 would be slightly underestimated for small NPs while it would be overestimated for large NPs. It can explain the few current spikes observed in the LSV constructed from the model and would indicate a catalytic efficiency fluctuating with NP size.

It should be stressed that reaching the intrinsic electrocatalytic activity of metallic Ni, besides at the single NP level, is a difficult task as it produces $Ni(OH)_2$ that will quickly coat the metallic Ni and will quickly reveal the influence of the $Ni(OH)_2$ coating on this activity. The final proposed mechanism is schematized in Figure 6c. This is clearly evidenced here as the Ni NP growth is halted rapidly because of the alteration of the growth process owing to the formation of a $Ni(OH)_2$ coating. The coated $Ni/Ni(OH)_2$ NP may still present an electrocatalytic activity which may be seen from the reduction current branch following the

Ni reduction peak. However, this activity is orders of magnitude smaller than that of pure Ni. For comparison, the k_0 value evaluated here, in agreement with previous estimates, is of the same order of magnitude as that of Pt metal.[74]

3. Conclusions

Electrochemistry in a micro-sized droplet cell is coupled to a correlative multi-microscopy strategy assisted by machine vision concepts. In the latter strategy, optical, electron and local probe microscopies work synergistically to provide highly complementary information on a complex electrochemical interface, that is electrode supported Ni based NPs. Optical microscopy monitors *operando* the NP nucleation and growth, while SEM and AFM image *ex situ* the deposit and provide the full 3D NP geometry. The collected data are analyzed by unsupervised machine learning, leading to the classification of all the NPs produced over the electrode surface (~1000 NPs or >5 10^8 NP/cm^2) based on their size and chemical composition without the need of the most time consuming or destructive analyses such as extensive EDX or AFM. By knowing precisely the position, size, growth dynamics and structure of all NPs, one can bridge the gap between these microscopic descriptors and the macroscopic electrochemical curve. The results then clearly highlighted the dramatic impact of the competing reactions (water and oxygen reduction) that occur during the NPs formation. Employing a droplet cell has been decisive, as it allowed downscaling the system and visualizing all the nanoobjects that are responsible of the electrochemical response. Particularly, this local to global strategy is pertinent since it allows determining the intrinsic electrocatalytic activity of highly reactive catalysts, illustrated here in the case of metallic Ni NPs. Beyond demonstrating the importance of highly sensitive single entity electrochemistry measurement, or high spatial resolution electrochemical imaging techniques, it shows the significance of confronting it to ensemble macroscale measurements in order to reveal new mechanistic insights.

Supporting Information

Supporting Information is available from the Wiley Online Library.

Experimental details, data processing (describing how to operate the provided Python program routines with supplementary optical movie, SEM image database), benchmarking of clustering methods, optical simulation and influence of NP geometry on the flux (**pdf)**

Optical movie **(avi)**

SEM images database folder (**tif**)

Data processing program routines (**py**)

Acknowledgements

This work was partially financially supported by the ANR JCJC program (PIRaNa project, ANR-20-CE42-0001) and through the CNRS and Université Paris Cité. The authors acknowledge the ITODYS SEM facility, the Ile-de-France region and IDEX for financial support of the AFM-Beam-Rex platform.

Received: ((will be filled in by the editorial staff))

Revised: ((will be filled in by the editorial staff))

Published online: ((will be filled in by the editorial staff))

References

[1] Z. W. Seh, J. Kibsgaard, C. F. Dickens, I. Chorkendorff, J. K. Nørskov, T. F. Jaramillo, *Science* **2017**, *355*, eaad4998.

[2] S. E. F. Kleijn, S. C. S. Lai, M. T. M. Koper, P. R. Unwin, *Angew. Chem. Int. Ed.* **2014**, *53*, 3558.

[3] C. Costentin, C. Di Giovanni, M. Giraud, J.-M. Savéant, C. Tard, *Nat. Mater.* **2017**, *16*, 1016.

[4] J. Ustarroz, I. M. Ornelas, G. Zhang, D. Perry, M. Kang, C. L. Bentley, M. Walker, P. R. Unwin, *ACS Catal.* **2018**, *8*, 6775.

[5] A. R. Akbashev, *ACS Catal.* **2022**, *12*, 4296.

[6] T. Bligaard, R. M. Bullock, C. T. Campbell, J. G. Chen, B. C. Gates, R. J. Gorte, C. W. Jones, W. D. Jones, J. R. Kitchin, S. L. Scott, *ACS Catal.* **2016**, *6*, 2590.

[7] D. Voiry, M. Chhowalla, Y. Gogotsi, N. A. Kotov, Y. Li, R. M. Penner, R. E. Schaak, P. S. Weiss, *ACS Nano* **2018**, *12*, 9635.

[8] C. Wei, R. R. Rao, J. Peng, B. Huang, I. E. L. Stephens, M. Risch, Z. J. Xu, Y. Shao-Horn, *Adv. Mater.* **2019**, *31*, 1806296.

[9] D. Li, C. Batchelor-McAuley, R. G. Compton, *Appl. Mater. Today* **2020**, *18*, 100404.

[10] T. A. A. Batchelor, T. Löffler, B. Xiao, O. A. Krysiak, V. Strotkötter, J. K. Pedersen, C. M. Clausen, A. Savan, Y. Li, W. Schuhmann, J. Rossmeisl, A. Ludwig, *Angew. Chem. Int. Ed.* **2021**, *60*, 6932.

[11] M. R. Nellist, F. A. L. Laskowski, J. Qiu, H. Hajibabaei, K. Sivula, T. W. Hamann, S. W. Boettcher, *Nat. Energy* **2018**, *3*, 46.

[12] Y. Yang, Y. Xiong, R. Zeng, X. Lu, M. Krumov, X. Huang, W. Xu, H. Wang, F. J. DiSalvo, Joel. D. Brock, D. A. Muller, H. D. Abruña, *ACS Catal.* **2021**, *11*, 1136.

[13] S. Lui, Y. Ying, Y. Long, *Chin. Chem. Lett.* **2020**, *31*, 473.

[14] H. Wang, T. He, Y. Du, W. Wang, Y. Shen, S. Li, X. Zhou, F. Yang, *Chin. Chem. Lett.* **2020**, *31*, 2442.
[15] M. Lin, Y. Zhou, L. Bu, C. Bai, M. Tariq, H. Wang, J. Han, X. Huang, X. Zhou, *Small* **2021**, *17*, 2007302.
[16] J. T. Mefford, A. R. Akbashev, M. Kang, C. L. Bentley, W. E. Gent, H. D. Deng, D. H. Alsem, Y.-S. Yu, N. J. Salmon, D. A. Shapiro, P. R. Unwin, W. C. Chueh, *Nature* **2021**, *593*, 67.
[17] C. L. Bentley, M. Kang, P. R. Unwin, *J. Am. Chem. Soc.* **2019**, *141*, 2179.
[18] L. A. Baker, *J. Am. Chem. Soc.* **2018**, *140*, 15549.
[19] J. H. K. Pfisterer, Y. Liang, O. Schneider, A. S. Bandarenka, *Nature* **2017**, *549*, 74.
[20] M. Zhou, J. E. Dick, A. J. Bard, *J. Am. Chem. Soc.* **2017**, *139*, 17677.
[21] J. Linnemann, K. Kanokkanchana, K. Tschulik, *ACS Catal.* **2021**, *11*, 5318.
[22] J. A. Trindell, Z. Duan, G. Henkelman, R. M. Crooks, *Chem. Rev.* **2020**, *120*, 814.
[23] F. Kanoufi, in *Encyclopedia of Electrochemistry*, John Wiley & Sons, Ltd, **2021**, pp. 1–80.
[24] J.-F. Lemineur, H. Wang, W. Wang, F. Kanoufi, *Annu. Rev. Anal. Chem.* **2022**, *15*, DOI 10.1146/annurev-anchem-061020-015943.
[25] Y. Ma, A. L. Highsmith, C. M. Hill, S. Pan, *J. Phys. Chem. C* **2018**, *122*, 18603.
[26] P. Saha, J. W. Hill, J. D. Walmsley, C. M. Hill, *Anal. Chem.* **2018**, *90*, 12832.
[27] X. Shan, I. Díez-Pérez, L. Wang, P. Wiktor, Y. Gu, L. Zhang, W. Wang, J. Lu, S. Wang, Q. Gong, J. Li, N. Tao, *Nat. Nanotechnol.* **2012**, *7*, 668.
[28] J.-F. Lemineur, P. Ciocci, J.-M. Noël, H. Ge, C. Combellas, F. Kanoufi, *ACS Nano* **2021**, *15*, 2643.
[29] R. Hao, Y. Fan, M. D. Howard, J. C. Vaughan, B. Zhang, *Proc. Natl. Acad. Sci. U.S.A.* **2018**, *115*, 5878.
[30] S. Xu, X. Yu, Z. Chen, Y. Zeng, L. Guo, L. Li, F. Luo, J. Wang, B. Qiu, Z. Lin, *Anal. Chem.* **2020**, *92*, 9016.
[31] L. Godeffroy, P. Ciocci, A. Nsabimana, M. Miranda Vieira, J.-M. Noël, C. Combellas, J.-F. Lemineur, F. Kanoufi, *Angew. Chem. Int. Ed.* **2021**, *60*, 16980.
[32] D. Valavanis, P. Ciocci, G. N. Meloni, P. morris, J.-F. Lemineur, I. J. McPherson, F. Kanoufi, P. R. Unwin, *Faraday Discuss.* **2022**, *233*, 122.
[33] P. Unwin, *Faraday Discuss.* **2022**, *233*, 374.
[34] J. J. Gooding, K. Gaus, *Angew. Chem. Int. Ed.* **2016**, *55*, 11354.
[35] J.-F. Lemineur, J.-M. Noël, D. Ausserré, C. Combellas, F. Kanoufi, *Angew. Chem. Int. Ed.* **2018**, *57*, 11998.
[36] J.-M. Noël, J.-F. Lemineur, *Curr. Opin. Electrochem.* **2021**, *25*, 100647.
[37] W. Wang, *Chem. Soc. Rev.* **2018**, *47*, 2485.
[38] N. Ebejer, A. G. Güell, S. C. S. Lai, K. McKelvey, M. E. Snowden, P. R. Unwin, *Annu. Rev. Anal. Chem.* **2013**, *6*, 329.
[39] L. I. Stephens, N. A. Payne, S. A. Skaanvik, D. Polcari, M. Geissler, J. Mauzeroll, *Anal. Chem.* **2019**, *91*, 3944.
[40] M. Tuck, L. Blanc, R. Touti, N. H. Patterson, S. Van Nuffel, S. Villette, J.-C. Taveau, A. Römpp, A. Brunelle, S. Lecomte, N. Desbenoit, *Anal. Chem.* **2021**, *93*, 445.
[41] A. Mistry, A. A. Franco, S. J. Cooper, S. A. Roberts, V. Viswanathan, *ACS Energy Lett.* **2021**, *6*, 1422.
[42] L. B. Coelho, D. Zhang, Y. Van Ingelgem, D. Steckelmacher, A. Nowé, H. Terryn, *npj Mater. Degrad.* **2022**, *6*, 1.
[43] L. Mill, D. Wolff, N. Gerrits, P. Philipp, L. Kling, F. Vollnhals, A. Ignatenko, C. Jaremenko, Y. Huang, O. De Castro, J.-N. Audinot, I. Nelissen, T. Wirtz, A. Maier, S. Christiansen, *Small Methods* **2021**, *5*, 2100223.

[44] X. Wang, J. Li, H. D. Ha, J. C. Dahl, J. C. Ondry, I. Moreno-Hernandez, T. Head-Gordon, P. A. Alivisatos, *J. Am. Chem. Soc. Au* **2021**, *1*, 316.
[45] M. Ceriotti, *J. Chem. Phys.* **2019**, *150*, 150901.
[46] L. I. Stephens, N. A. Payne, J. Mauzeroll, *Anal. Chem.* **2020**, *92*, 3958.
[47] H. Chen, D. Li, E. Kätelhön, R. Miao, R. G. Compton, *Anal. Chem.* **2022**, *94*, 5901.
[48] P. Puthongkham, S. Wirojsaengthong, A. Suea-Ngam, *Analyst* **2021**, *146*, 6351.
[49] V. Vij, S. Sultan, A. M. Harzandi, A. Meena, J. N. Tiwari, W.-G. Lee, T. Yoon, K. S. Kim, *ACS Catal.* **2017**, *7*, 7196.
[50] J. Clausmeyer, J. Masa, E. Ventosa, D. Öhl, W. Schuhmann, *Chem. Commun* **2016**, *52*, 2408.
[51] N. Danilovic, R. Subbaraman, D. Strmcnik, K.-C. Chang, A. P. Paulikas, V. R. Stamenkovic, N. M. Markovic, *Angew. Chem. Int. Ed.* **2012**, *51*, 12495.
[52] R. Subbaraman, D. Tripkovic, D. Strmcnik, K.-C. Chang, M. Uchimura, A. P. Paulikas, V. Stamenkovic, N. M. Markovic, *Science* **2011**, *334*, 1256.
[53] N. L. Ritzert, T. P. Moffat, *J. Phys. Chem. C* **2016**, *120*, 27478.
[54] R. Wang, U. Bertocci, H. Tan, L. A. Bendersky, T. P. Moffat, *J. Phys. Chem. C* **2016**, *120*, 16228.
[55] Z. Liang, H. S. Ahn, A. J. Bard, *J. Am. Chem. Soc.* **2017**, *139*, 4854.
[56] M. P. Zach, R. M. Penner, *Adv. Mater.* **2000**, *12*, 878.
[57] J. C. Crocker, D. G. Grier, *J. Colloid Interface Sci.* **1996**, *179*, 298.
[58] S. Suzuki, K. Abe, *Comput. graph. image process.* **1985**, *30*, 32.
[59] P. Ciocci, J.-F. Lemineur, J.-M. Noël, C. Combellas, F. Kanoufi, *Electrochim. Acta* **2021**, *386*, 138498.
[60] L. Liu, S. Yellinek, I. Valdinger, A. Donval, D. Mandler, *Electrochim. Acta* **2015**, *176*, 1374.
[61] S. Geiger, O. Kasian, A. M. Mingers, K. J. J. Mayrhofer, S. Cherevko, *Sci. Rep.* **2017**, *7*, 4595.
[62] O. J. Wahab, M. Kang, G. N. Meloni, E. Daviddi, P. R. Unwin, *Anal. Chem.* **2022**, *94*, 4729.
[63] V. Sundaresan, J. W. Monaghan, K. A. Willets, *J. Phys. Chem. C* **2018**, *122*, 3138.
[64] N. Y. Molina, T. Pungsrisai, Z. J. O'Dell, B. Paranzino, K. A. Willets, *ChemElectroChem* **2022**, *9*, e202200245.
[65] C. Amatore, J. M. Savéant, D. Tessier, *J. Electroanal. Chem.* **1983**, *147*, 39.
[66] M. E. Hyde, R. G. Compton, *J. Electroanal. Chem.* **2003**, *549*, 1.
[67] N. Godino, X. Borrisé, F. X. Muñoz, F. J. del Campo, R. G. Compton, *J. Phys. Chem. C* **2009**, *113*, 11119.
[68] J.-F. Lemineur, J.-M. Noël, C. Combellas, F. Kanoufi, *J. Electroanal. Chem.* **2020**, *872*, 114043.
[69] L. Heerman, A. Tarallo, *J. Electroanal. Chem.* **1999**, *470*, 70.
[70] O. Orrick, M. Yang, C. Batchelor-McAuley, R. G. Compton, *J. Electroanal. Chem.* **2021**, *900*, 115738.
[71] Zbigniew. Stojek, Janet. Osteryoung, *Anal. Chem.* **1989**, *61*, 1305.
[72] J. Ustarroz, J. A. Hammons, T. Altantzis, A. Hubin, S. Bals, H. Terryn, *J. Am. Chem. Soc.* **2013**, *135*, 11550.
[73] H. E. M. Hussein, R. J. Maurer, H. Amari, J. J. P. Peters, L. Meng, R. Beanland, M. E. Newton, J. V. Macpherson, *ACS Nano* **2018**, *12*, 7388.
[74] P. J. Rheinländer, J. Herranz, J. Durst, H. A. Gasteiger, *J. Electrochem. Soc.* **2014**, *161*, F1448.